IAEA-F1-CN-69/TH3/4

3D MHD SIMULATIONS OF PELLET INJECTION AND DISRUPTIONS IN TOKAMAK PLASMAS

H.R. STRAUSS
New York University, New York, NY, USA
W. PARK, E. BELOVA, G.Y. FU
Princeton Plasma Physics Laboratory, Princeton, NJ, USA
L.E. SUGIYAMA
Massachusetts Institute of Technology, Cambridge, MA, USA

Abstract

Nonlinear MHD simulation results of pellet injection show that MHD forces can accelerate large pellets, injected on the high field side of a tokamak, to the plasma center. Magnetic reconnection can produce a reverse shear q profile. Ballooning instability caused by pellets is also reduced by high field side injection. Studies are also reported of the current quench phase of disruptions, which can cause 3D halo currents and runaway electrons.

1. MHD EFFECTS ON PELLET INJECTION

Nonlinear MHD simulations of pellet injection [1] are in qualitative agreement with recent ASDEX results [2]. Pellets injected on the inboard, low major radius side tend to penetrate into the plasma, while pellets injected on the outboard side tend to be expelled. Efficient pellet penetration is important for very large size, long pulse tokamaks, such as ITER.

A scaling law is obtained for pellet displacement which agrees well with the simulations. The MHD simulations were carried out with the new MH3D++ unstructured mesh finite element version of the MH3D full MHD code [3].

The simulations are initialized with a two dimensional MHD equilibrium, to which a pellet is added. The simulations assume that the pellet ionizes and ablates rapidly, compared to the sound wave transit time scale. The pellet is the source of a plasma cloud, which has a non uniform density and pressure distribution on magnetic surfaces. The pellet cloud contributes no energy to the plasma; the flux surface averaged pressure profile is the same as without the pellet. The three dimensional perturbed non equilibrium plasma relaxes by parallel streaming of heat and density, and major radius displacement akin to the Shafranov shift. Driven magnetic reconnection imparts some non reversibility to the effect.

When a pellet is injected into a plasma, the pellet rapidly heats, and ablates. The ablated gas then ionizes and becomes a cloud of high density plasma, which is cooler than its surroundings. The plasma cloud moves together with the background plasma, according to the dissipative MHD equations,

$$\frac{\partial \mathbf{B}}{\partial t} = \nabla \times (\mathbf{v} \times \mathbf{B} - \eta \nabla \times \mathbf{B}) \tag{1}$$

$$\rho \frac{d\mathbf{v}}{dt} = (\nabla \times \mathbf{B}) \times \mathbf{B} - \nabla p + \mu \nabla^2 \mathbf{v} \tag{2}$$

where $p = \rho T$, η is the resistivity and μ a scalar viscosity. The density satisfies the continuity equation. A single temperature, the electron temperature, is assumed for simplicity. The temperature transport parallel to the magnetic field, which tends to make the temperature approximately constant on magnetic field lines, is modeled with the "artificial sound" method [1,4].

In principle, the injection process is adiabatic, imparting no energy to the plasma. The temperature is constant on flux surfaces before and after the pellet injection. After injection, the temperature is lower on flux surfaces that intersect the pellet cloud. To calculate the new temperature, adiabaticity implies that the flux surface average $< p >$ of the pressure p remains the same, before and after the pellet injection. The pellet - perturbed density $\delta\rho$ is not constant

on a flux surface. Hence p is far from constant on flux surfaces, and the plasma is out of MHD equilibrium.

The subsequent motion of the plasma was studied in numerical simulations. The computations were done on a poloidal mesh of about 2000 grid points, and at least 9 toroidal Fourier harmonics in addition to the $n = 0$ mode. The plasma is assumed bounded by a rigid conducting wall. An initial equilibrium was prepared, starting with a prescribed initial, non equilibrium state, and evolving in 2D, removing kinetic energy, until an equilibrium is approached. In the following cases, the equilibrium has a rotational transform at the magnetic axis $q_0 = 1.7$, initial peak $\beta = 0.06a/R$, and the aspect ratio $R/a = 5$. In addition, the pressure is boosted an additional constant amount with $\beta = 0.3a/R$. This additional constant pressure enhances the sound speed, while having no effect on the background magnetic equilibrium. This makes the total peak $\beta = 0.36a/R$. The initial equilibrium density is constant.

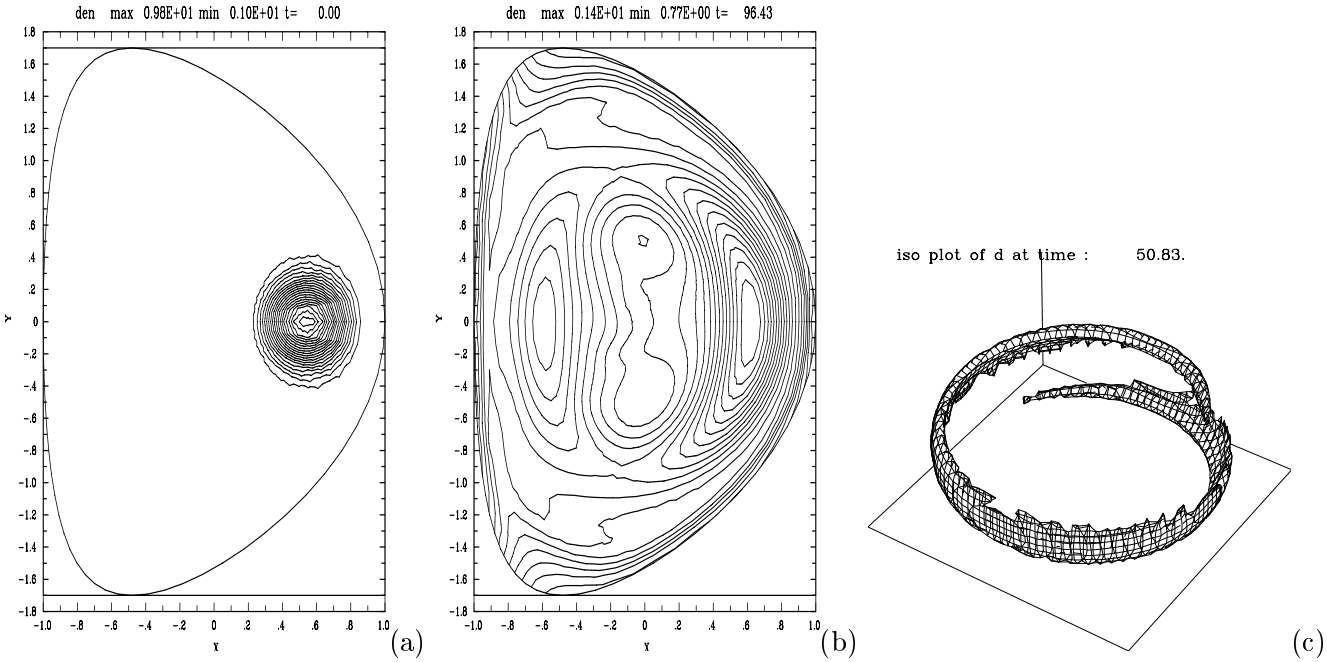

Figure 1: (a) initial density contours showing the pellet in the poloidal plane $\phi = 0$, at the outboard side of the equilibrium. (b) density contours at $t = 96\tau_A$ as the pellet moves outward and spreads poloidally. (c) density isoplot at $t = 51\tau_A$ showing the pellet cloud spreading out along the magnetic field.

The initial equilibrium was perturbed with a density blob representing the ionized pellet ablation cloud. In the following, the blob's peak density is 15 times the background density. The blob is cigar shaped, with a circular cross section in the poloidal plane, and a dependence on toroidal angle ϕ proportional to $\sim \cos^4(\phi/2)$. The density perturbation extends roughly 1/4 of the way around the torus. The model ablation cloud is considerably less localized than in experiments. This was done because of constraints on numerical resolution, that should be relaxed in future simulations. Similarly the density contrast is less than in experiments. However, the total mass of the pellet, which is a few percent of the total background plasma, is comparable to experimental cases. The effects demonstrated here are expected to be sufficiently robust to qualitatively account for experimental observations.

Since the flux surface averaged pressure $< p >$ is the same with and without the pellet, there is a tendency to return to the initial equilibrium state after the pellet cloud spreads out on magnetic field lines. However, when reconnection occurs, the plasma tends toward a new equilibrium.

All other things being equal, the 3D evolution depends on the initial location of the pellet

perturbation in the poloidal plane, as well as the pellet density. In the case of outboard injection, the initial density ρ is shown in Fig.1(a), in the plane $\phi = 0$ where the density is a maximum. The pellet is located at the outboard midplane. The density contours at $t = 96\tau_A, \phi = 0$ are shown in Fig.1(b), where $\tau_A = R/v_A$, the toroidal Alfvén transit time, R is the major radius, and v_A is the Alfvén speed. The density has moved both outwards in major radius, as well as spreading out laterally. Part of the pellet also appears on the inboard side. This is caused by spreading along the magnetic field, as shown in an isoplot of the density at $t = 51\tau_A$, in Fig.1(c).

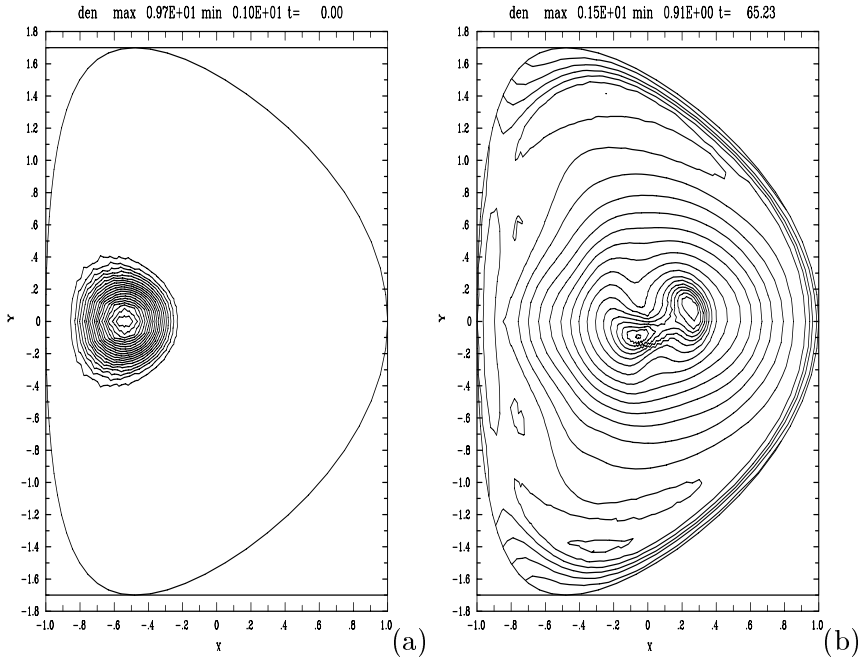

Figure 2: (a) initial density contours showing the pellet in the poloidal plane $\phi = 0$, at the inboard side of the equilibrium. (b) density contours at $t = 65\tau_A$ as the pellet penetrates to the plasma center.

In the case of inboard injection, the initial density blob is located at the inboard midplane, shown in in Fig.2(a). The density at $t = 65\tau_A, \phi = 0$, is shown in Fig.2(b). The pellet has reached the plasma center. To get to this state, the density blob had to cut magnetic field lines, by the process of driven magnetic reconnection. Accordingly, the run was performed with resistivity $\eta = 2 \times 10^{-4} a^2 v_A/R$. The effect requires that the parallel sound transit time is longer than or comparable to the reconnection time. This seems to be the case in present day large tokamaks, for which the reconnection rate is anomalous. The $q(\psi)$ profiles at the times shown in Fig.2, are shown in Fig.3(a). The pellet has reconnected magnetic flux to produce a reversed magnetic shear profile. The $q(\psi)$ profile at $t = 65\tau_A$ was generated using the toroidally averaged magnetic flux ψ, but at this time the magnetic asymmetry is small. This process might be used to maintain a reversed shear configuration, as well as for deep fueling of ITER like large tokamaks, where pellets are expected to be ablated close to the surface.

The displacement of the pellet can be measured by calculating the change in flux surface $\delta\psi/\psi$ of the peak of the flux surface averaged density $< \rho >$, using the toroidally averaged magnetic flux. An approximate expression for the maximum pellet displacement can be derived [1]

$$\frac{\delta\psi}{\psi} \approx -\beta q^2 \frac{R}{a} \left(\frac{\delta a}{a}\right)^2 (1 + \frac{\delta a}{a\delta\phi})^{-1} \frac{\delta p}{p_0} \cos\theta \tag{3}$$

where δp is the pellet pressure, δa is the pellet radius, $\delta\phi$ measures the extent of the pellet cloud in the toroidal angle ϕ, $\beta = 2p_0/B^2$, and p_0 is the background pressure. Plugging in $\beta R/a = .30, \delta p/p_0 = 10, \delta a = .2a, q = 2.0$, and $\delta\phi = \pi/2$, gives the dotted straight line in

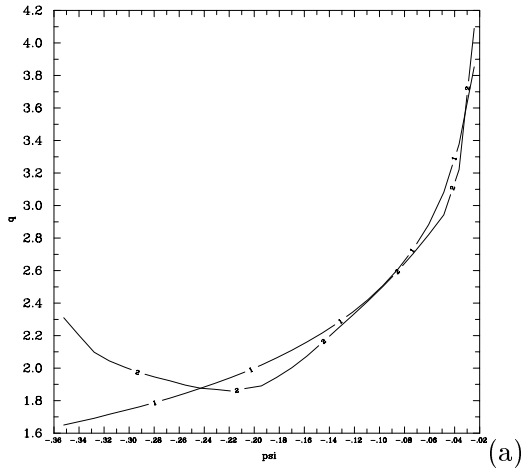

(a)

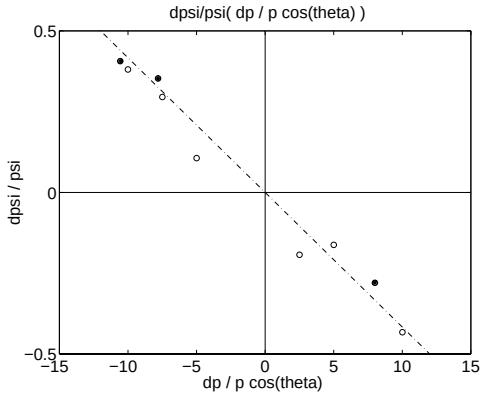

(b)

Figure 3: (a) $q(\psi)$ profile at times (1)$t = 0$, (2)$t = 65\tau_A$. Penetration of the pellet has reconnected the magnetic field and produced a reversed shear q profile. (b) theory and simulation results of maximum pellet displacement as a function of $\delta\rho/\rho \cos\theta$, where θ is the poloidal angle of the pellet's initial position. Outboard is $\theta = 0$, inboard is $\theta = \pi$.

Fig.2(c). The data is collected in Fig.3(b), which plots the maximum shift $\delta\psi/\psi$ as a function of $(\delta p/p_0)\cos\theta$. Several cases, marked with unfilled circles, were initialized with a simple non adiabatic model, in which the temperature was not modified to give an invariant pressure profile. The maximum displacement (3) is proportional to $\delta p(\delta a)^2$, which is proportional to the pellet mass [1]. The left most point in Fig.2(c), the inboard injection case, has the maximum possible deviation $\delta\psi/\psi$, the pellet having penetrated to the center.

2. MHD DISRUPTIONS CAUSED BY PELLET INJECTION

Inboard pellet injection also confers advantages with regards to MHD stability of the background plus pellet system. Because of the high local β at the pellet cloud, the system may be unstable to pressure driven modes, even though the background equilibrium is stable. Pellets on the outboard side tend to be more destabilizing, because the pellet pressure gradient and the equilibrium gradient add on the large R side of the equilibrium. With inboard injection, the pressure gradients oppose one another. In addition, on the low field side, the velocity perturbations resemble typical moderate wavelength ballooning modes. They produce disruptions in nonlinear simulations. On the high field side, the velocity perturbations are much more localized. They might simply cause the breakup and more rapid dispersion of the pellet cloud.

A high β equilibrium was produced, with peak $\beta = .25a/R$. The equilibrium becomes unstable if β is increased to $.30a/R$. The q profile varied from 1.7 on axis to 3.7 at the wall, and $R/a = 3$. The D shaped boundary was the same as in the previous section.

This was modified by the presence of a pellet perturbation. The density perturbation had localization similar to that of the previous section, but now varied as $\cos^2\phi$ for improved numerical resolution. The amplitude of the density perturbation was varied, with the temperature and density perturbations initialized as before. This time, the low toroidal mode number part of the MHD equations were not allowed to evolve, only modes with mode number $n > 4$. This was done to try to separate the equilibrium evolution, described above, from higher mode number, faster growing instabilities.

Inboard and outboard pellet perturbations were centered on approximately the same flux surface, so that a given density perturbation produced the same amplitude pressure perturbation. An outboard pellet is considered in Fig.4. The initial pressure profile as a function of major radius, $p(R)$, through the maximum of the pellet pressure perturbation, is shown in Fig.4(a). The density perturbation is $\delta\rho/\rho = 15$. The shape of the unstable modes is shown in Fig.4(b) showing contours of electrostatic potential for an outboard pellet perturbation. This mode has

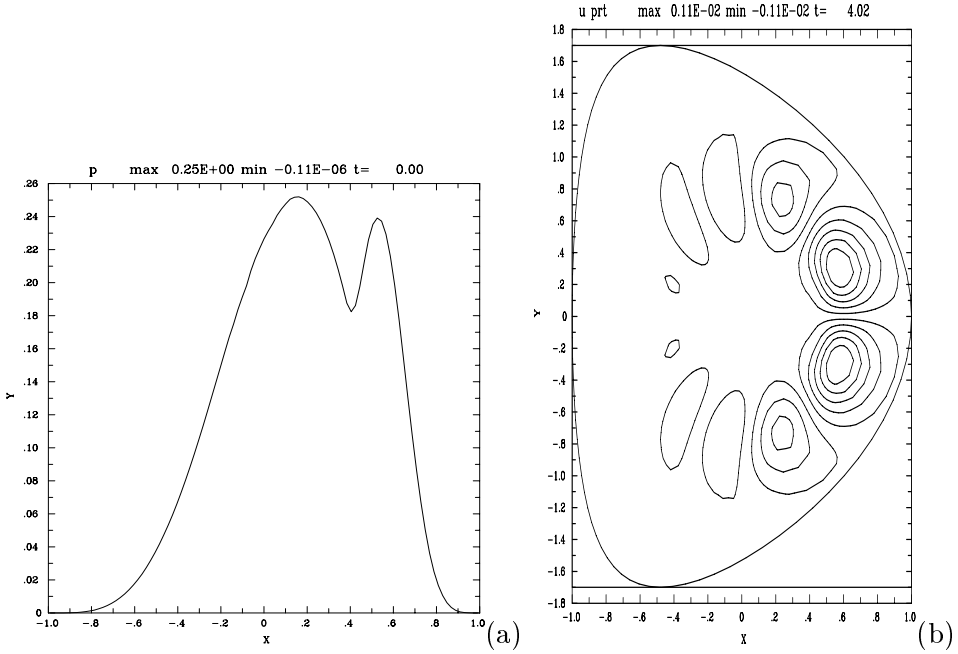

Figure 4: (a) pressure as a function of major radius through the center of the pellet. (b) Contours of electrostatic potential for outboard pellet.

a mixture of toroidal mode numbers, centered at $n = 5$. The mode has a ballooning structure, and is toroidally localized, but poloidally less localized than the following inboard injection case. This is similar to nonlinear destabilization by n=1 pressure perturbations during disruptions.[5]

In comparison, an inboard pellet is shown in Fig.5. The pressure profile is shown in Fig.5(a). The density perturbation is twice as large, $\delta\rho/\rho = 30$, and so is the pressure perturbation. A perturbation of the same amplitude as in Fig.4(a) is marginally unstable for an inboard pellet. The electrostatic potential contours of the unstable mode are shown in Fig.5(b). The mode is more localized to the pellet, because outside the pellet, the pressure gradient is in the same direction as the curvature, which is stabilizing. This difference appears to persist in nonlinear runs, using the pellet and linear modes as perturbations of the background equilibrium. In this case too, inboard injection is more favorable, because the instability threshold $\delta\rho/\rho$ is higher, and because the unstable modes are more localized.

3. DISRUPTIONS, HALO CURRENTS, AND RUNAWAYS

Another category of work with MH3D++, which is relevant to ITER and other large tokamaks, concerns halo currents and runaways generated during the current quench phase following major disruptions. Halo currents caused by 3D kink modes in the latter phases of a disruption could cause serious mechanical load problems. In addition, runaway electron currents could be channeled to the wall by the 3D magnetic field perturbations, causing wall damage. Disruption simulations are being carried out which have both a self consistent three dimensional resistivity proportional to the temperature to the $-3/2$ power, as well as a thin resistive shell through which the plasma magnetic field is coupled to an external vacuum field. Runaway generation by avalanche is also modeled based on Ref. 6.

The plasma is bounded by an inner, thin, resistive shell of thickness δ and resistivity η_w. Surrounding this is an outer vacuum region, enclosed by an outer, conducting wall. In the vacuum region, the magnetic field is source free and determined by boundary conditions on the outer and inner walls. The vacuum boundary condition on the inner wall is found by integrating $\nabla \cdot \mathbf{B}$ across the thin shell, $\hat{n} \cdot [[\mathbf{B}]] = 0$, where the double bracket indicates a jump across the thin wall, and $\hat{n}$ is the unit normal (pointing outward from the plasma.) The boundary conditions on the plasma side of the boundary are given by the tangential components of the

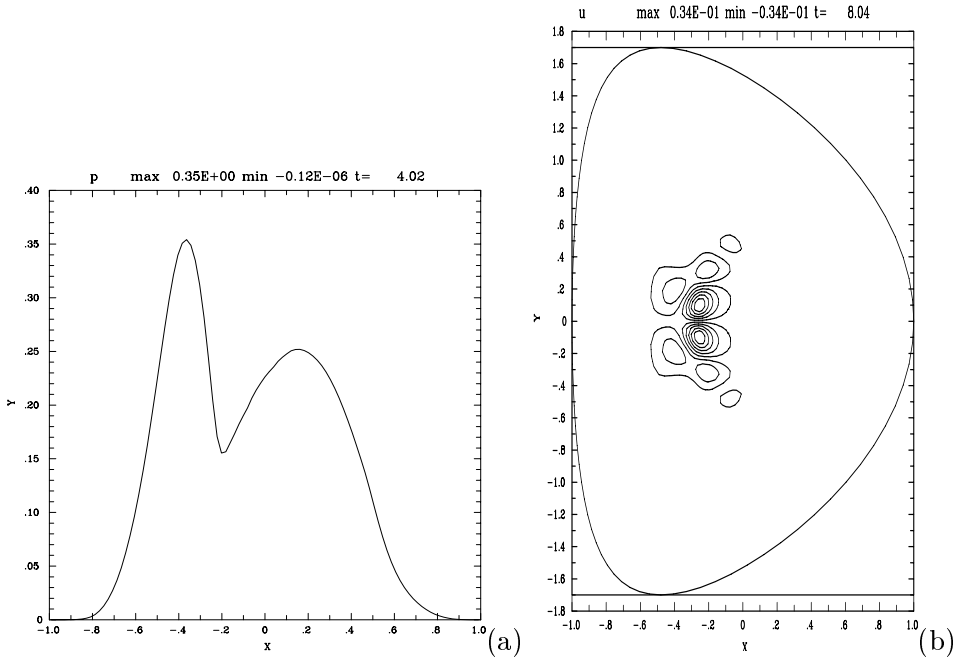

Figure 5: (a) pressure as a function of major radius through the center of the pellet. (b) Contours of electrostatic potential for inboard pellet.

electric field, $\mathbf{E} = \eta\mathbf{J}$. In the wall, $\mathbf{J} = (1/\delta)\hat{n} \times [[\mathbf{B}]]$, so the electric field at the plasma edge is $\mathbf{E} = (\eta_w/\delta)\hat{n} \times [[\mathbf{B}]]$.

The initial state is a resistive equilibrium with a current channel, having $q = .8$ on axis. The conducting shell has an average radius about 1.5 times that of the thin resistive shell. The equilibrium is unstable to an $n = 1$ kink. As the kink evolves nonlinearly, the radial component of the poloidal current is measured. The radial component is typically only 10% of the tangential component at the wall. The peak radial poloidal current is about 10% of the initial toroidal current on axis.

When the runaways are included, the results are similar. The evolution time is somewhat slowed, as the runaway parameter is increased. The model used is based on a local approximation of equations given in [6], with the convection term and parallel propagation terms added;

$$E_{||} = \eta(j_{||} - ecn_R) \tag{4}$$

$$\frac{\partial n_R}{\partial t} = \gamma_R n_R \left(\frac{E_{||}}{E_c} - 1\right) f(\frac{E_{||}}{E_c}) - \nabla \cdot (n_R \mathbf{V}_\perp) + c\mathbf{B} \cdot \nabla v/B \tag{5}$$

$$\frac{\partial v}{\partial t} = c\mathbf{B} \cdot \nabla(n_R/B) \tag{6}$$

where $\gamma_R = eE_c/(mc \ln\Lambda)$ and $f(x) = [1 - 1/x + c_2/(x^2 + c_3)]^{-1/2}$. The constant $E_c = 4\pi e^3 n_e \ln\Lambda/(mc^2)$ is here normalized as $E_c = \alpha\eta B/(cR)$, with α chosen such that the avalanche time $1/\gamma_R = 0.03\tau_R$. The "artificial sound" terms, eq. 6 and the last term of eq. 5, represent propagation along the field lines with speed of light c.[4]

In the following simulation, the resistive time is $\tau_R = 0.5 \times 10^4 \tau_A$. The wall time $\tau_w = .002\tau_R$, where $\tau_w = \delta a/\eta_w$, with δ/a the ratio of wall thickness to plasma radius. The time scales are in the order $\tau_R >> 1/\gamma_R >> \tau_w >> \tau_A$.

A test simulation is shown in Fig.6. The initial toroidal current density j_ϕ contours are shown in Fig.6(a), in the poloidal plane $\phi = 0$. At time $t = 18.5\tau_A$, which is far into the nonlinear evolution, the j_ϕ contours at $\phi = 0$ appear as in Fig.6(b). The peak current is on the wall, where the peak value of the normal component of poloidal current j_n is also located.

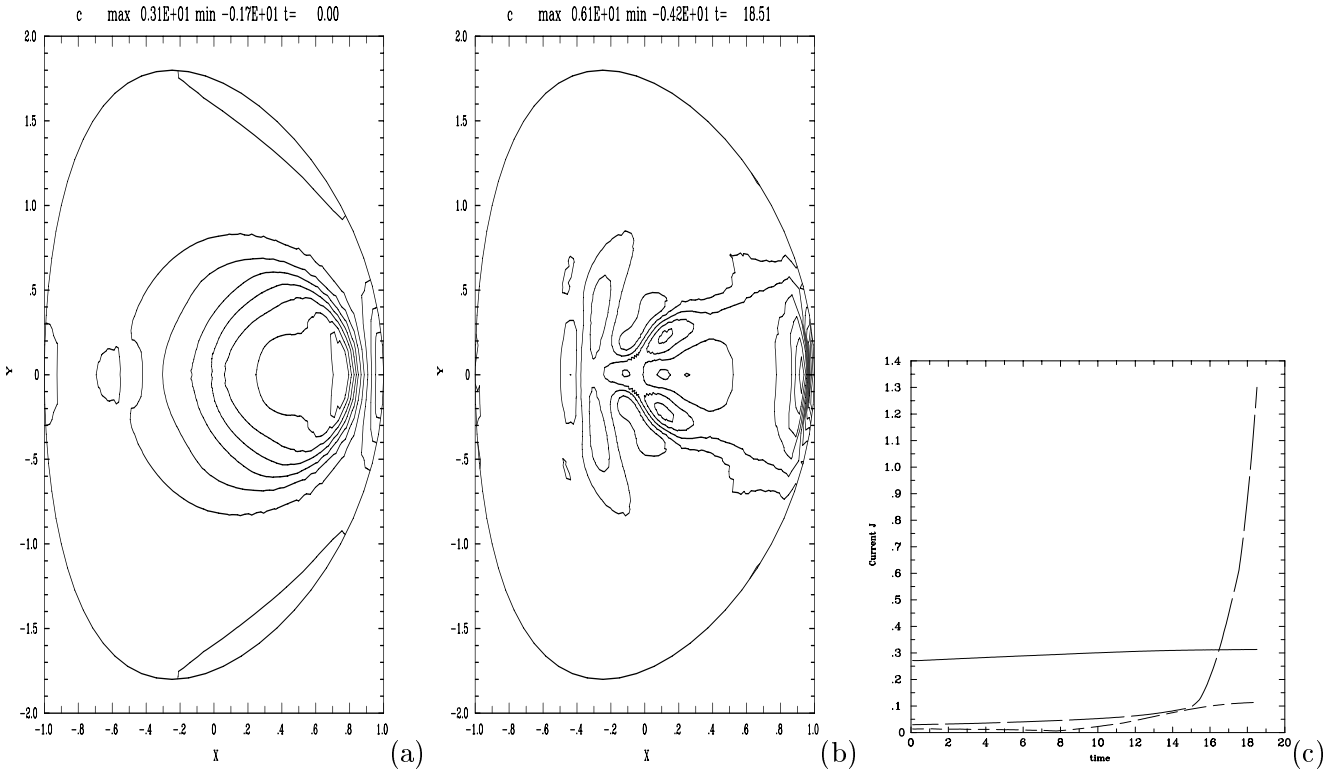

Figure 6: (a) Initial toroidal current contours in a kink unstable resistive equilibrium. (b) Contours of current density in nonlinear phase of instability. (c) Time history of: peak n=0 component of radial current at the wall (short - dashed line), peak n=0 component of runaway toroidal current (long - dashed line), average toroidal current density (solid line).

A time history of the peak $n = 0$ component of j_n, $j_R = ecn_R$, and the poloidal average of the $n = 0$ component of j_ϕ are shown in Fig.6(c), where n is toroidal mode number. The ratio of peak $n = 0$ and $n = 1$ components of radial poloidal current at the wall is close to unity, so that the peaking factor is about 2. Contours of the runaway part of the current are shown in Fig.7(a). In this simulation, the parallel propagation terms have not been included. These terms would equilibrate the runaway density on magnetic flux surfaces, and cause losses along open field lines. The total runaway current fraction in this simulation is about 15%.

4. MH3D++ UNSTRUCTURED MESH CODE

The most efficient way to represent general geometric effects is to use an unstructured numerical mesh. MH3D++ is the unstructured mesh finite element version of the MH3D code. The MH3D++ code is a part of the larger M3D code package[3], so that non-MHD kinetic effects can be included in the future simulations. The currently available physics models of the M3D project are MHD, two-fluids, and gyrokinetic ion/fluid electron hybrid models.

MH3D++ replaces the original finite difference - spectral discretization, with an unstructured mesh and finite element [7] - spectral discretization. The unstructured mesh is made with triangular and quadrilateral cells, as shown in Fig.7(b). The MHD equations are discretized with piecewise linear finite elements, The differential operators in the equations become sparse matrices involving integrals of the basis functions and their derivatives. The finite element unstructured mesh discretization has been incorporated into MH3D++ with an object oriented approach. The unstructured mesh objects generate an unstructured mesh and produce the sparse matrices which implement differential operators including gradient, curl, and divergence, as well as various Poisson solvers based on an Incomplete Cholesky Conjugate Gradient solver. Also included are mesh operations needed for line integration and contour plots. Routines which perform differential operations and solve elliptic PDEs are encapsulated in C++ objects

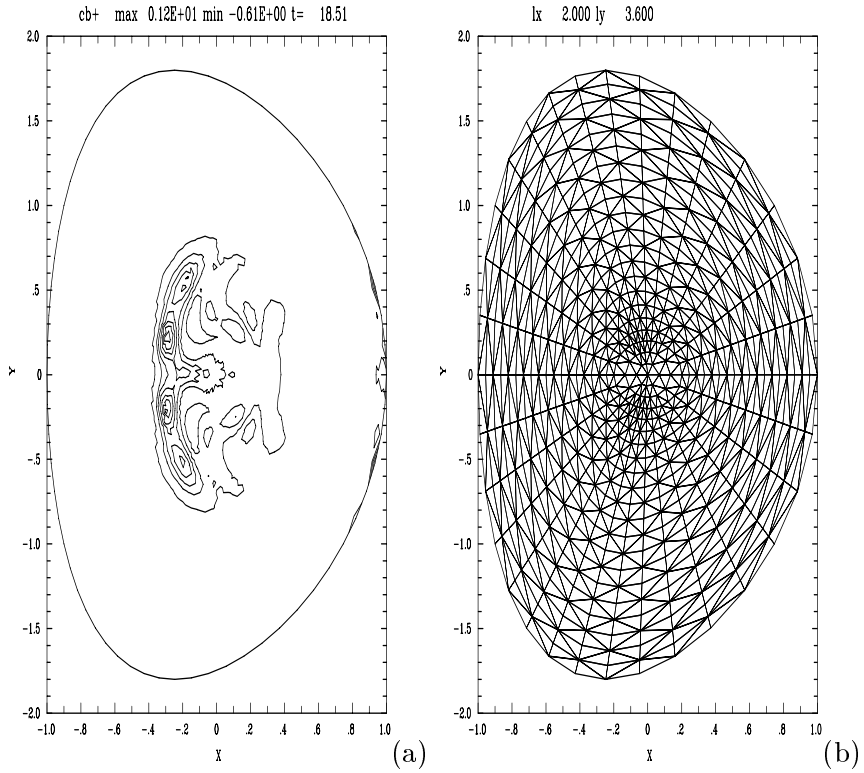

Figure 7: (a) Contours of runaway current in nonlinear phase of instability. (b) Poloidal unstructured mesh with 1/4 of the mesh points used in the simulations.

to isolate the finite element operations from higher level routines. In this way, the code can be run either in unstructured or in structured mesh versions, which still holds advantages for some specific problems.

An important feature of this approach is that most of the MH3D code is retained. This allows direct benchmarking of the two versions against each other. Equilibrium and stability calculations using the two versions have been compared, and the MH3D++ and MH3D results converge to each other. With the object oriented approach, it is straightforward to make arrays of mesh objects. Two mesh objects were used in the simulations of the previous section: one for the plasma interior mesh, and one for the vacuum region.

The MH3D++ code has been given an option of a finite difference discretization in the toroidal direction, replacing the spectral representation. This permits efficient parallelization. The next step, using an array of mesh objects to build a three dimensional mesh, has been carried out and is being tested for resistive, nonlinear stellarator simulations.

Acknowledgements

This work was supported by U.S. DoE grant DE-FG02-86ER53223 and contract DE-AC02-76-CHO-3073.

References

[1] STRAUSS, H. , PARK, W., Phys. Plasmas 5 (1998) 2676.

[2] LANG, P.T., BUECHL, K., KAUFMANN, M., *et al.,* Phys. Rev. Lett. 79 (1997) 1487.

[3] PARK, W., CHANG, Z., FREDRICKSON, E, FU, G. Y., POMPHREY, N., STRAUSS, H. R., SUGIYAMA, L. E., 16th IAEA Fusion Energy Conference, Montreal (1996) F1-CN-64/D2-2.

[4] PARK, W., MONTICELLO, D., STRAUSS, H., MANICKAM, Phys. Fluids **29** (1986) 1171.

[5] PARK, W., *et al.,* Phys. Rev. Lett. **75** (1995) 1763.

[6] ROSENBLUTH, M. N., PUTVINSKI, S. V., Nuclear Fusion 37, (1997) 1355.

[7] STRAUSS, H. R., LONGCOPE, D. W., Journal of Computational Physics 147, 1-19 (1998).